

HI 21cm observations and dynamical modelling of the thinnest galaxy: FGC 2366

K. Aditya¹ \star , Arunima Banerjee¹ \dagger , Peter Kamphuis², Aleksandr Mosenkov^{3,4}, Dmitry Makarov⁵ Sviatoslav Borisov^{5,6,7}

¹ Department of Physics, Indian Institute of Science Education and Research (IISER) Tirupati, Tirupati - 517507, India

² Ruhr Universität Bochum, Astronomisches Institut, Universitätsstrasse 150, D-44801 Bochum, Germany

³ Department of Physics and Astronomy, N283 ESC, Brigham Young University, Provo, UT 84602, USA

⁴ Pulkovo Observatory, Russian Academy of Sciences, St. Petersburg, 196140 Russia

⁵ Special Astrophysical Observatory, Russian Academy of Sciences, Nizhni Arkhyz, 369167 Russia

⁶ Sternberg Astronomical Institute, M.V. Lomonosov Moscow State University, Universitetsky prospect 13, Moscow, 119234 Russia

⁷ Department of Astronomy, University of Geneva, Chemin Pegasi 51, 1290 Versoix, Switzerland

28 August 2023

ABSTRACT

Superthin galaxies are bulgeless low surface brightness galaxies with unusually high major-to-minor axes ratio of the stellar disc, i.e., $10 < a/b < 20$. We present Giant Metrewave Radio Telescope (GMRT) HI 21cm radio-synthesis observations of FGC 2366, the thinnest galaxy known with $a/b = 21.6$. Employing the 3-D tilted-ring modelling using Fully Automated TiRiFiC (FAT), we determine the structure and kinematics of the HI gas disc, obtaining an asymptotic rotational velocity equal to 100 km s^{-1} and a total HI mass equal to $10^9 M_{\odot}$. Using z -band stellar photometry, we obtain a central surface brightness of $22.8 \text{ mag arcsec}^{-2}$, a disc scale length of 2.6 kpc, and a scale height of 260 pc. Next, we determine the dark matter density profile by constructing a mass model and find that an NFW dark matter halo best fits the steeply-rising rotation curve. With the above mass inventory in place, we finally construct the dynamical model of the stellar disc of FGC 2366 using the stellar dynamical code "AGAMA". To identify the key physical mechanisms responsible for the superthin vertical structure, we carry out a Principal Component Analysis of the data corresponding to all the relevant dynamical parameters and a/b for a sample of superthin and extremely thin galaxies studied so far. We note that the first two principal components explain 80% of the variation in the data, and the significant contribution is from the compactness of the mass distribution, which is fundamentally responsible for the existence of superthin stellar discs.

Key words: galaxies: individual, galaxies: FGC 2366, galaxies: kinematics and dynamics, galaxies: structure, method: data analysis

1 INTRODUCTION

Superthin galaxies are bulgeless edge-on disc galaxies with low surface brightness, i.e., with central surface brightness in the B -band $\mu_B(0) > 22.7 \text{ mag arcsec}^{-2}$ (Bothun et al. 1997; McGaugh 1996) and characterized by large values of the major-to-minor axes ratio a/b i.e., $10 < a/b < 22$ (Karachentsev et al. 1999). For a review of properties of superthin galaxies, see Matthew et al. (2000) and Kautsch (2009). Superthin galaxies have been studied in various observational surveys like the SDSS (Kautsch et al. 2006; Bizyaev et al. 2017; Bizyaev

et al. 2021). The Revised Flat Galaxy Catalogue (RFGC), sourced from the Palomar Observatory Sky Survey (POSS-II) survey, is the primary catalogue of edge-on disc galaxies (Karachentsev et al. 1999). It contains 4,444 edge-on galaxies with $a/b > 7$, 1150 galaxies with an $a/b > 10$, and only 6 extremely thin galaxies with $a/b > 20$, indicating the paucity of extremely thin galaxies. In Figure 1, we show the distribution of the a/b ratio of the RFGC population. We see that the extremely thin galaxies constitute the tail of the distribution of the RFGC. The term *superthin* was first used by Goad & Roberts (1981) for galaxies with a/b in the range 9 - 20. Karachentseva et al. (2016) classify the galaxies in the RFGC with $a/b > 10$ as *ultra-flat* galaxies and use the term interchangeably with the *superthin* galaxy, which is

\star E-mail: kaditya@students.iisertirupati.ac.in

\dagger E-mail: arunima@iisertirupati.ac.in

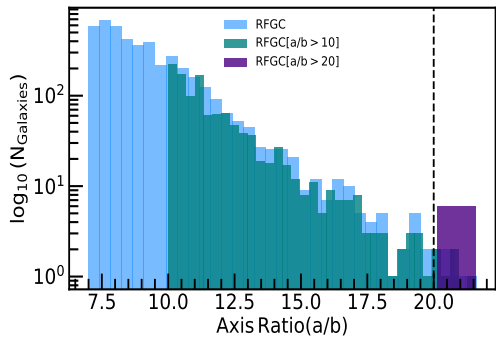


Figure 1. Distribution of the RFGC galaxies with respect to the major-to-minor axes ratio a/b of their stellar discs. The vertical line demarcates the superthin galaxies (Left) from extremely thin galaxies (Right).

also the nomenclature adopted in the review by [Kautsch \(2009\)](#). [Matthews et al. \(1999\)](#) use the ratio of the vertical exponential scaleheight of the stellar disc-to-the radial disc scalelength $h_z/R_d \leq 0.1$ as the definition of *superthin* galaxies. In this work, we use the term *extremely thin galaxies* to refer to RFGC galaxies with $a/b > 20$ and the term *superthin* for $10 < a/b < 20$. Although superthin galaxies are ubiquitous, as indicated in Figure 1, curiously, the number of superthin and extremely thin galaxies produced in the Λ cold dark matter (Λ CDM) simulations is not significant. In a recent study, [Haslbauer et al. \(2022\)](#), measured the sky-projected aspect ratio distribution in the Λ CDM simulations: IllustrisTNG ([Pillepich et al. 2018](#)), and EAGLE ([Schaye et al. 2015](#)) and found that these simulations are deficient in galaxies with intrinsically thin discs. (Also see [Vogelsberger et al. \(2014\)](#) and [Bottrell et al. \(2017\)](#)).

Our current understanding of the superthin galaxies is mostly derived from the detailed dynamical modelling of a limited sample of superthin galaxies using stellar photometry available in the literature and HI 21cm radio-synthesis observations. Most of these galaxies have $10 < a/b < 16$, i.e. UGC 7321 ([O’Brien et al. 2010](#); [Banerjee & Jog 2013a](#)), IC5249 ([van der Kruit et al. 2001](#); [O’Brien et al. 2010](#)), IC 2233 ([Matthews & Uson 2008](#)), FGC 1540 ([Kurapati et al. 2018](#)). HI 21cm observations in edge-on galaxies offer a two-fold constraint on the net gravitational potential of the galaxy, i.e. the rotation curve constraining the radial derivative, and the vertical gas thickness the vertical derivative of the same ([Olling 1995](#); [Narayan & Jog 2002](#)). Using disc dynamical stability arguments, [Zasov et al. \(1991\)](#) showed that a massive dark matter halo stabilizes a superthin disc. Besides, [Ghosh & Jog \(2014\)](#) showed that the prototypical superthin galaxy UGC 7321 is stable against local, axisymmetric and non-axisymmetric perturbations due to its dark matter halo. [Banerjee et al. \(2010\)](#) argued that UGC 7321 is dominated by dark matter at all galactocentric radii, and [Banerjee & Bapat \(2017\)](#) found that superthin galaxies have compact dark matter halos, i.e., $R_c/R_d < 2$ where R_c is the core radius of a pseudo-isothermal dark matter halo and R_d the exponential stellar disc scale length. Besides, [Banerjee & Jog \(2013b\)](#) argued that a compact dark matter halo plays a decisive role in regulating the thin vertical structure of the stellar disc. Further, the razor-thin vertical structure of

the superthin galaxies indicates the presence of an ultra-cold stellar disc. This may also be the reflection of a highly anisotropic stellar velocity ellipsoid with relatively less heating in the vertical as compared to the radial direction ([Quinn et al. 1993](#); [Khoperskov et al. 2003](#); [Purcell et al. 2010](#); [Gentile et al. 2015](#); [Grand et al. 2016](#)). However, the vertical component of the stellar velocity dispersion of superthin galaxies is not directly measurable from the observations, given their edge-on orientation. Using a sample of five superthin galaxies with $a/b < 16$, [Aditya & Banerjee \(2021\)](#) theoretically determined the stellar vertical velocity dispersion as a function of the radius using the observed scaleheight of the stellar disc as one of the constraints, and found the ratio of the vertical velocity dispersion to the radial velocity dispersion lying between 0.3 – 0.5 in comparison to a value of ~ 0.5 as seen in ordinary disc galaxies. Also, the ratio of the vertical velocity dispersion to rotational velocity was found to be comparable to the Galactic thin disc. Finally, basic physics suggests that a high value of the planar-to-vertical axes ratio of the stellar disc could be the outcome of a high value of the specific angular momentum of the disc. Interestingly, [Jadhav Y & Banerjee \(2019\)](#) found that superthin galaxies have a relatively high specific angular momentum at a given mass compared to bulgeless ordinary disc galaxies as given in [Romanowsky & Fall \(2012\)](#), indicating the possibility of a high value of specific angular momentum driving the superthin stellar discs.

In this paper, we choose the thinnest galaxy, FGC 2366, for its first-ever HI 21cm radio-synthesis observations using the Giant Meterwave Radio Telescope (GMRT), followed by modelling the structure and kinematics of HI using the 3D tilted ring modelling software Fully Automated TiRiFiC (FAT, [Kamphuis et al. \(2015\)](#)). We model the HI rotation curve and HI surface density, which, along with stellar photometry available in the literature, was used for mass modelling and detailed dynamical modelling of these galaxies. We focus on four dynamical quantities that may be instrumental in driving the strikingly high planar-to-vertical axes ratios in these galaxies, namely, the 1) Dark matter density profile, 2) Stellar vertical velocity dispersion, and the ratio of the vertical-to-radial stellar velocity dispersion, 3) Disc dynamical stability against local axisymmetric perturbations 4) Specific angular momentum of the disc. We then compare and contrast the above physical parameters of FGC 2366 with those of the previously studied extremely thin galaxy FGC 1440, other superthins, and ordinary disc galaxies. Finally, we do a Principal Component Analysis of a set of dynamical parameters corresponding to our sample of superthins and extremely thin galaxies to identify the key dynamical mechanism responsible for the superthin vertical structure of their stellar discs. The rest of the paper is organised as follows; in §2, we introduce the target FGC 2366; in §3, we describe the HI observations, data reduction, analysis, and 3-D tilted ring modelling, and in §4, the optical photometry followed by the dynamical modelling and conclusions in §5 and §6 respectively.

2 FGC 2366

FGC 2366 is an extremely thin galaxy from the RFGC ([Karachentsev et al. 1999](#)). The ratio of the major-to-minor

Table 1. Basic astrophysical parameters of FGC 2366

| Parameter | Value |
|---------------------------------|---|
| RA(J2000) ^{(1)a} | 22 ^h 08 ^m 03 ^s .62 |
| Dec(J2000) ^{(1)b} | -10°19′59″.1 |
| Hubble type ^{(1)c} | Sd |
| i ^{(3) c} | 90° |
| Distance ⁽⁴⁾ | 32.95 Mpc |
| a/b ^{(1)d} | 21.6 |
| log(M_{HI}) ^{(2)e} | 9.38 |
| W_{50} ^{(5)f} | 204.5 |

^a Right ascension

^b Declination

^c Inclination

^d Major axis to minor axis ratio

^e HI mass

^f Spectral line width at 50% of the peak flux density

(1): Karachentsev et al. (1999)

(2): Matthews & van Driel (2000)

(3): Makarov et al. (2014)

(4): Kourkchi et al. (2020)

(5): This Work

axes for FGC 2366 is equal to 21.6, which makes it the thinnest or the flattest known galaxy. FGC 2366 was observed as part of the survey of 472 late-type, edge-on spiral galaxies using Nancy Radio Telescope and the Green Bank Telescope by Matthews & van Driel (2000); an integrated HI flux density equal to 5.93 Jy km s⁻¹, and velocity width at 50% of peak flux (W_{50}) equal to 188 km s⁻¹ were reported. The basic properties of FGC 2366 are presented in Table 1.

3 HI 21CM RADIO-SYNTHESIS OBSERVATIONS

We observed FGC 2366 using GMRT on 25 August 2019, for 9 hours, including overheads and with 27 working antennae. The source was observed for 7 hours through 14 scans of half an hour each, interspersed by 14 scans of the phase calibrator 2136+006 for 5 minutes each. The flux calibrator 3C286 was observed at the beginning, and another, 3C48, at the end of the observation for half an hour. We have observed the central frequency of 1406.9 MHz in GSB mode with 512 channels with a total bandwidth of 4.2 MHz and a spectral resolution of 8.14 kHz. A velocity resolution of 1.7 km s⁻¹ allows us to model the dispersion of the gas as well as to cover the full velocity extent of the galaxy. HI emissions in multiple channels allows us to construct realistic 3D model of the galaxy using FAT, see §3.2. We use the Common Astronomy Software Application (CASA) (McMullin et al. 2007) for data reduction. We start by flagging off the bad antennae (E04, E05, E06) from our data set and then visually inspect and flag the data corrupted by radio frequency interference (RFI). We then follow the usual procedure for cross-calibration before splitting off the target from the measurement set. Thereafter, we make a dirty cube to locate the channels with spectral line emission and flag off those channels to constitute a continuum-only measurement set. Next, we perform 5 rounds of phase-only self-calibration and four rounds of amplitude-phase self-calibration, each time applying the self-calibration solutions to the measurement

Table 2. HI observations of FGC 2366: Technical specifications

| (a) Observing Setup | |
|---------------------------------------|---|
| Parameter | Value |
| Observing Date | 25 August 2019 |
| Phase center, α (J2000) | 22 ^h 08 ^m 03 ^s .62 |
| Phase center, δ (J2000) | -10°19′59″.1 |
| Total on-source observation time | 5.5 hrs |
| Flux calibrator | 3C286, 3C48 |
| Phase calibrator | 2136+006 |
| Channel Width | 8.14 kHz |
| Velocity separation | 1.7 km s ⁻¹ |
| Central frequency | 1406.9 MHz |
| Total bandwidth | 4.2 MHz |
| (b) Deconvolved Image Characteristics | |
| Weighing | robust |
| Robustness parameter | 0.5 |
| Synthesized beam FWHM | 13.4″ × 11.7″ |
| Synthesized beam position angle | 39.4° |
| rms noise in channel | 0.39 mJy/beam |

set. The signal-to-noise ratio (S/N) saturates after about 5 rounds of phase-only self-calibration. During amplitude-phase self-calibration, the image quality initially deteriorates but improves after the second round, and the S/N ratio saturates after the third round. We apply the final amplitude-phase self-calibration table to the target-only measurement set. We then subtract the continuum, excluding the channels containing the spectral line, with a zeroth order interpolation excluding the spectral channels. We then make a dirty cube using the continuum subtracted measurement set and create a mask using the Source Finding Algorithm (SoFiA: Serra et al. (2015)). Finally, we cleaned the dirty cube using a mask made using SoFiA to the final data cube. Upon experimenting, we found that ‘briggs’ weighing scheme in the CASA task ‘tclean’ with robustness parameter equal to 0.5 and a uvtaper equal to 12kl gives the best compromise between sensitivity and resolution. The details of the observations and the deconvolved image characteristics are summarized in Table 2.

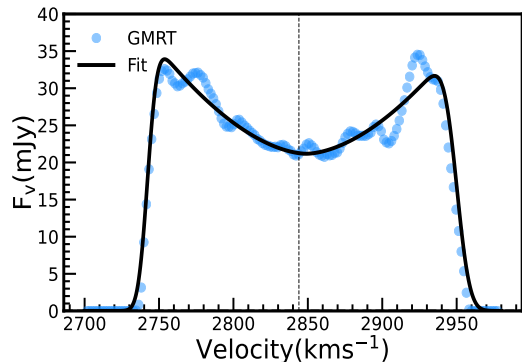
3.1 Data Analysis

In Figure 2, we present the global HI profile of FGC 2366. We fit the observed profile using the busy-function (Westmeier et al. 2014) and find that the integrated flux is equal to 5.4 Jy km s⁻¹ and the peak HI flux equal to 34 mJy. The integrated flux obtained by fitting the busy function to the HI spectrum is comparable to the flux measured directly from the data cube using the CASA task *SPECFLUX*. The integrated flux gives us a HI mass of galaxy equal to $\log_{10}(M_{HI}/M_{\odot}) = 9.1$. We find that the (W_{20}) and the (W_{50}) velocity widths are 214 km s⁻¹ and 205 km s⁻¹, respectively. The results obtained by fitting the busy function are shown in Table 3. In Figure 3, we show an integrated column density (Moment 0) map and the velocity field (Moment 1) for FGC 2366. We have overlaid the column density map on the POSS-II optical image of FGC 2366. We find that the Moment 0 map is smooth and unperturbed, and also, we do not find any enhanced emission from either the centre or the edge of the HI disc. Also, we note that the HI distribution and velocity field is similar to other superthin galaxies; for example, see Kurapati et al. (2018). In Figure 4, we present the images of channels con-

Table 3. Busy function fit to HI Global profile

| $V_0^{(a)}$ km s ⁻¹ | $W_{50}^{(b)}$ km s ⁻¹ | $W_{20}^{(c)}$ km s ⁻¹ | $F_{peak}^{(d)}$ mJy | $F_{int}^{(e)}$ Jy km s ⁻¹ |
|-----------------------------------|--------------------------------------|--------------------------------------|-------------------------|--|
| 2844 ± 2.4 | 204.5 ± 2.9 | 214.4 ± 3.9 | 33.9 ± 0.3 | 5.4 ± 0.2 |

- (a): Frequency centroid of the HI line.
(b): Spectral line width at 50% of the peak flux density.
(c): Spectral line width at 20% of the peak flux density.
(d): Peak of the HI flux density.
(e): Integrated HI flux.

**Figure 2.** Global HI profile of FGC 2366 derived from our GMRT radio-synthesis observation, with the best-fitting busy function, over-plotted. The vertical dashed line indicates the systemic velocity.

taining HI emission overlaid on the POSS-II optical image. For convenience, we have shown every fourth channel. We observe that the HI emission close to the systemic velocity and away from the systemic velocity lie along a flat plane. Only in the edge channels does the HI emission on both the approaching and the receding sides show a slight deviation away from the plane.

3.2 3D-Tilted Ring Modeling

We use the publicly available automated 3D-tilted ring modelling software Fully Automated TiRiFiC (FAT) (Kamphuis et al. 2015), which is a GDL wrapper around the tilted ring modelling software TiRiFiC (Józsa et al. 2007). TiRiFiC generates model data cubes from the tilted ring parametrization of the rotating disc and fits the model data cubes directly to the observed data cubes. Fitting the observed data cubes directly using TiRiFiC allows us to accurately derive the structural and kinematic properties of a completely edge-on galaxy like FGC 2366. This is otherwise not feasible using conventional 2D methods, which rely on the velocity field for the derivation of structural and kinematic properties and therefore suffer from effects arising from projection and beam smearing. The 2D velocity field is typically affected by beam smearing that affects the derivation of the rotation curve in the inner regions of the galaxy. In contrast, projection effects do not allow one to derive a unique velocity field for completely edge-on galaxies as the line-of-sight intersects the disc multiple times. These problems are circumvented by fitting directly to the observed data cube rather than fitting to derived data products like 2D-velocity fields or PV diagrams. FAT uses the HI data cube as input

and automates the fitting of the following free parameters: 1) surface brightness 2) position angle, 3) inclination, 4) rotational velocity, 5) scaleheight 6) intrinsic dispersion, and 7) central coordinates: right ascension, declination, and systemic velocity. Each of the free parameters can be fitted at every radial point independently. We divide the HI disc into two halves and fit 19 semi-rings across each half, with each semi-ring being 0.6 times the major axis beam size, and model the vertical gas distribution using the sech² profile. The best-fitting values obtained by fitting 3D models using FAT are shown in Table 4; the rotation curve, velocity dispersion, and the surface brightness profiles thus obtained are presented in Figure 5. The red and black lines indicate the surface brightness profiles of the approaching and the receding sides, respectively. From the HI surface brightness profile, we note the presence of the central HI hole, which could be due to supernova-driven outflows or conversion of the dense atomic gas in the centre into molecular hydrogen gas. In Figure 5, we note that the surface brightness peaks have a similar value but occur at a different radius. From the major axis PV diagram, we note that the approaching side has a slightly higher surface brightness than the receding. Thus, despite symmetric surface brightness maps, the asymmetry in the velocity space is reflected in radially integrated surface brightness profiles. Also, we find the 3D model of FGC 2366 constructed using FAT accurately describes the HI distribution except for the asymmetry at the highest contour, see Figure 7.

In Figure 6, we overlay the rotation curve derived using the 3D model on the major axis PV diagrams. We observe that the shape of the rotation curve derived from the 3D modelling agrees with the shape of the mid-plane emission in the PV diagram along the major axis. Further, from the PV diagram along the major axis, we note that the galaxy has a similar rotation curve for the approaching and the receding side. We observe that the central velocity estimated by FAT differs from that obtained by fitting the busy function as the FAT fits the 3D data cube directly. However, we may note here that we fit the busy function to the spectrum derived from the 3D cube, which is a 1D representation of the data. Further, the HI spectrum, as given in Figure 2, shows slight asymmetry, which could be a possible reason for the difference in the value of the central velocity obtained by FAT and busy function fitting. Further, we over-plot the emissions observed from channels at 2844 km s⁻¹ (estimated from the 1D spectrum) and 2832.5 km s⁻¹ (estimated from the 3D data cube using FAT). We find that the emission observed at 2832.5 km s⁻¹ coincides with the centre of the optical image. (See Figure 20 in Appendix A.) In Figure 6, we plot the systemic velocity estimated by FAT on the major axis PV diagram. We can clearly see that the systemic velocity estimated by FAT coincides with the centre of the galaxy. Throughout this work, we will use 2832.5 km s⁻¹ as the systemic velocity. Further, from Figure 6, we can see that the approaching side is brighter than the receding side, possibly indicating kinematic asymmetry, which is driving the difference between the values of systemic velocity estimated from 3D data cube using FAT and from the 1D spectrum.

We define the uncertainties on the observed rotation curve following Swaters et al. (2009) and De Blok et al. (2008). We quantify the two main sources of uncertainties on the rotation curve; one arising due to the difference in

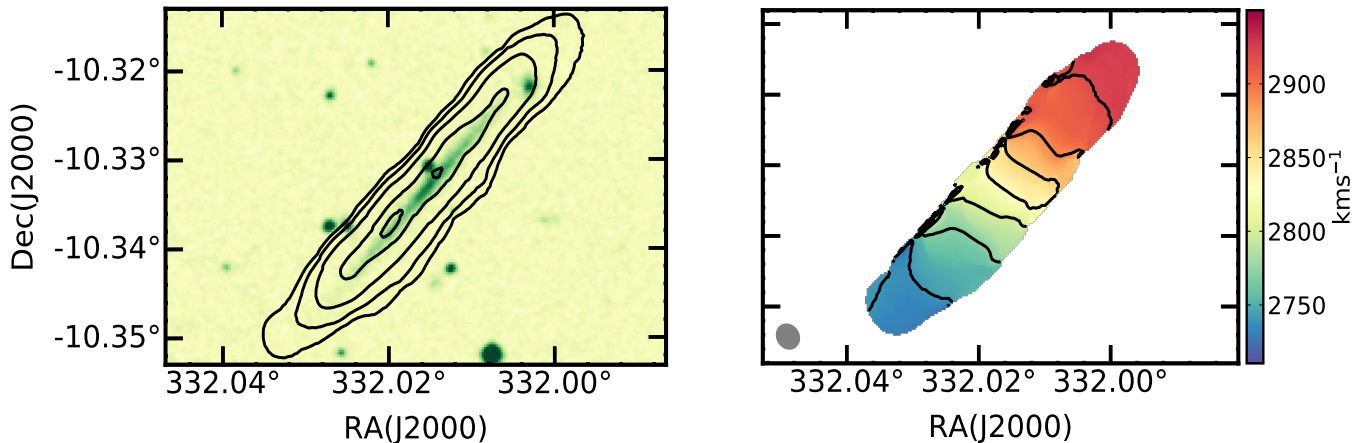


Figure 3. Moment 0 [Left] and Moment 1 [Right] maps derived from the observed HI data cube. The data contours are shown in black. The contours levels in the moment 0 maps at $[4.0, 8.0, 16, 32, 40] \times 10^{20}$ atoms cm^{-2} and the contours in the moment 1 map start at 2951 km s^{-1} and end at 2710 km s^{-1} increasing by 26 km s^{-1} .

the rotation velocities between the approaching and the receding sides and the second due to the spectral resolution of our observation. We define the final uncertainty by adding in quadrature the spectral resolution and one-fourth of the difference of the rotation velocity on the approaching and the receding side. Since we find a similar rotation velocity on the approaching and receding sides, the errors on our rotation curve are primarily the spectral resolution of our observation.

Quality of Fits: In Figure 7, we compare the Moment 0 and Moment 1 map derived from the input and model data cube. The black contours depict the data, and the crimson contours show the 3D model of the HI distribution generated by TiRiFiC. In Figure 7, we plot the velocity contours separated by 26 km s^{-1} so that we can have sufficient contours at the centre and away from the centre to compare the model and the data amenably. The model contours closely follow the observed HI distribution. The moment maps contain information about the surface brightness distribution and velocity separately, whereas the observed data cube has a three-dimensional structure. Therefore it is necessary to compare the minor axis PV diagrams, which preserve the 3D structure of the observed data cube. In Figure 8 [top panel], we compare the minor axis PV diagrams derived from the input data cube and the model data cube, and in the bottom panel, we present the residual plots. We have spatially smoothed the data cube for making the minor axis PV diagrams to allow for overall comparison between model and data amenable. Our model data cube reproduces the overall observed structure of the HI emission, and the difference between the model and the data arises only at velocities away from the galaxy close to 3σ .

4 OPTICAL PHOTOMETRY

We derive the structural parameters for FGC 2366 in the g , r , and z bands using optical images from the DESI Legacy Imaging Surveys DR9 (Dey et al. 2019). This galaxy does not exhibit an apparent dust lane or any traces of dust, even in the bluest optical bands. Therefore, to a first approxima-

Table 4. Best-fitting model derived by FAT

| Parameter | Values |
|-------------------------------|--|
| X_o ^a | $22^{\text{h}}08^{\text{m}}03^{\text{s}}.62$ |
| Y_o ^b | $-10^{\circ}19'59''.1$ |
| i ^c | $87.1^{\circ} \pm 4^{\circ}$ |
| V_{sys} ^d | 2832.5 km s^{-1} |
| PA ^e | $317.1^{\circ} \pm 2^{\circ}$ |
| h_z ^f | $6.7''$ |

- ^a Right ascension
- ^b Declination
- ^c Inclination
- ^d Systemic velocity
- ^e Position angle
- ^f Scaleheight of the HI disc

tion, we can neglect the internal extinction in this galaxy and roughly estimate its structural parameters for all three available bands. We use the publicly available photometric decomposition package IMFIT (Erwin 2015) and employ the ExponentialDisk3D function with the galaxy inclination parameter. We fit the light distribution keeping the central surface brightness, radial scalelength, vertical exponential scaleheight, and inclination as free parameters. The results of our decomposition for all three bands are shown in Table 5. We estimate the total magnitudes of the galaxy model in the g , r , and z bands, corrected for the Galactic extinction from Schlafly & Finkbeiner (2011), to be 15.44, 15.01, and 14.76, respectively. From Table 5, we can see that the radial scalelength decreases with wavelength, which conforms with the inside-out formation scenario. Unlike the disc scalelength, we find that the disc scaleheight is slightly smaller in the redder z -band than the g -band and the r -band, but the variation in the scaleheight is comparable within the error bars. The scale height in all three bands does not change within the error bars. The model and data profile along the major axis in the z -band are shown in Figure 9.

Mass-to-light ratio:

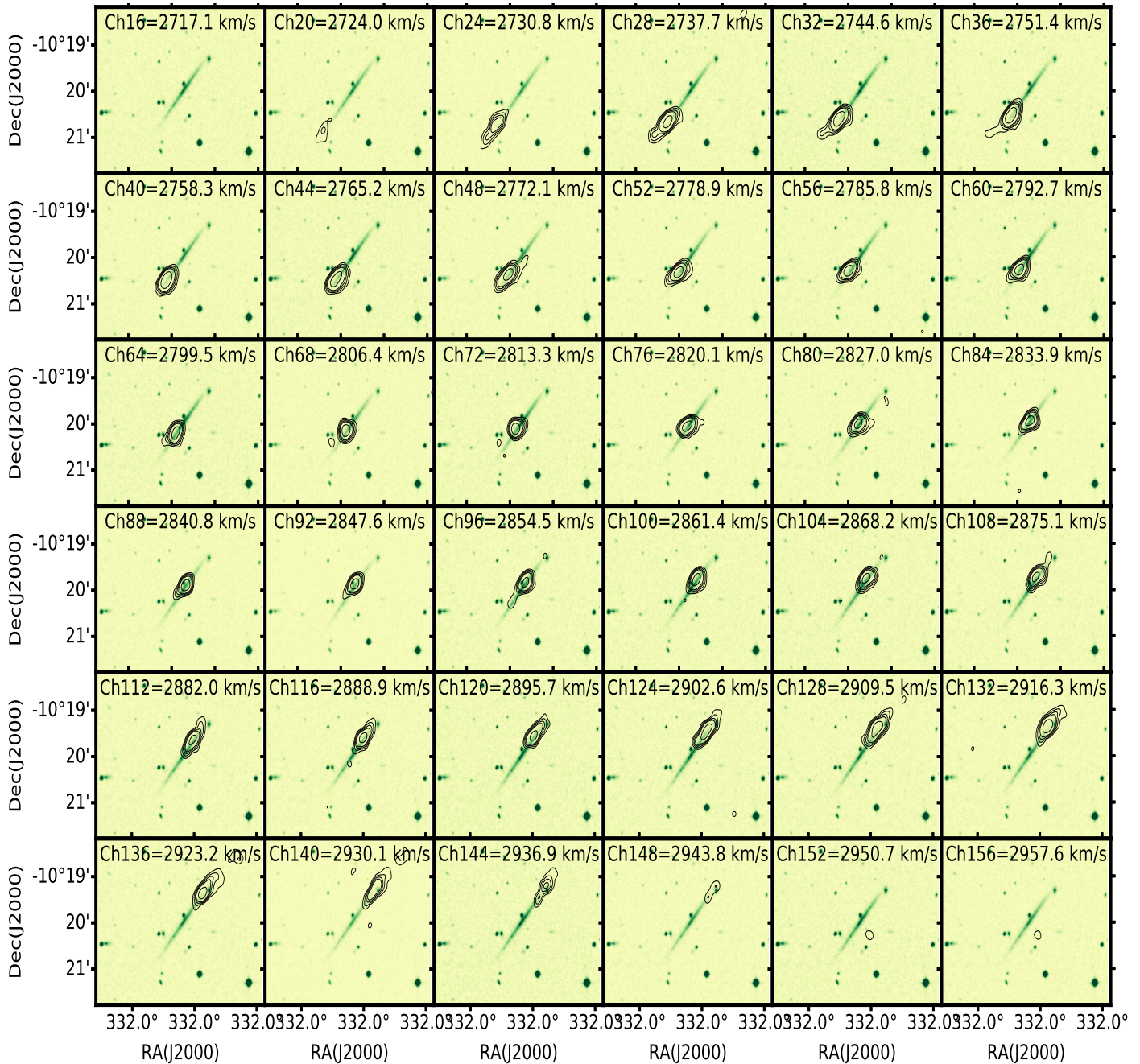


Figure 4. Channel maps showing HI emission from FGC 2366, each panel is separated by four channels. The HI emissions are overlaid on the POSS-II optical image. The contour levels are at $[3, 4, 5, 6, 9] \times 0.8 \text{ mJy beam}^{-1}$

We derive the mass-to-light ratio in the z-band in order to convert the surface brightness profile in L_{\odot}/pc^2 unit to the surface density profile in M_{\odot}/pc^2 using the calibration given in Bell et al. (2003a). The empirical calibration between the colour and the mass to the light ratio in a given band is given as $\log_{10}(M/L) = a_{\lambda} + b_{\lambda}(Color)$. We use the g-z magnitudes to derive the colour and the values of a_z and b_z tabulated in Bell et al. (2003b) and compute the mass-to-light ratio in the z band. The details are presented in Table 6.

We use the z-band photometry for constructing the mass models as it is a better tracer of the total stellar luminosity than the g and the r bands. Using the values of the a_{λ}

and b_{λ} corresponding to the z-band photometry, we find an M/L value equal to 1.1 using a scaled Salpeter initial mass function (IMF). Palunas & Williams (2000), using I-band photometry for a sample of 75 spiral galaxies, find $M/L = 2.4 \pm 0.9$. Using K-band photometry McGaugh & Schombert (2014) show that the M/L remains fairly constant at 0.6 for spiral galaxies.

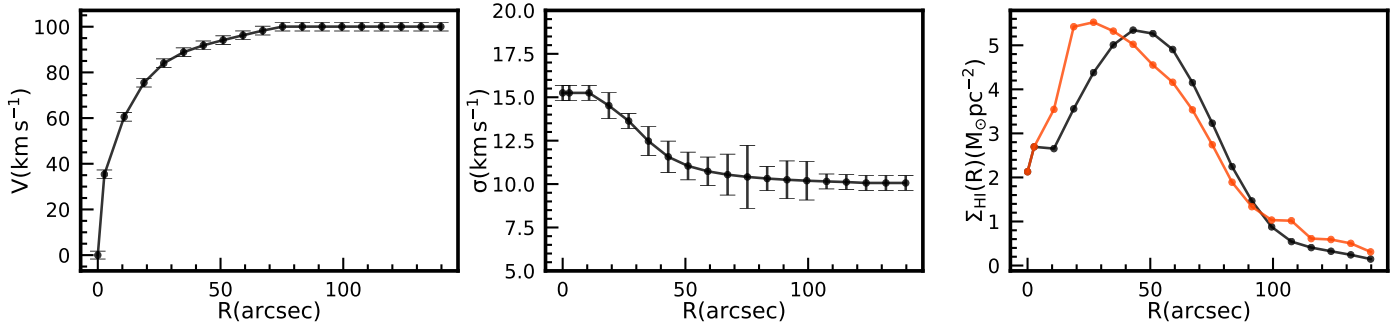


Figure 5. Best-fitting model derived using the 3-D tilted modelling of the observed HI data cube. [Left Panel] Rotational velocity [Middle Panel] HI dispersion [Right Panel] HI surface density as a function of galactocentric radii. The red and black lines in the right panel indicate the surface brightness profile of the approaching and receding sides, respectively.

Table 5. Structural parameters derived from optical photometry of FGC 2366.

| Parameter | g-band | r-band | z-band | Description |
|-------------------|------------------|------------------|------------------|---|
| Total magnitude | 15.44 | 15.01 | 14.76 | |
| $\mu_o^{edge-on}$ | 21.58 ± 0.02 | 20.97 ± 0.02 | 20.46 ± 0.02 | Edge-on surface brightness ($\text{mag}/\text{arcsec}^2$) |
| R_d | 20.4 ± 0.2 | 17.9 ± 0.1 | 16.1 ± 0.1 | Disc scalelength (arcsec) |
| h_z | 2.0 ± 0.1 | 2.0 ± 0.1 | 1.8 ± 0.1 | Disc scaleheight (arcsec) |
| i | 89.3 ± 0.1 | 89.0 ± 0.1 | 88.6 ± 0.1 | (degrees). |

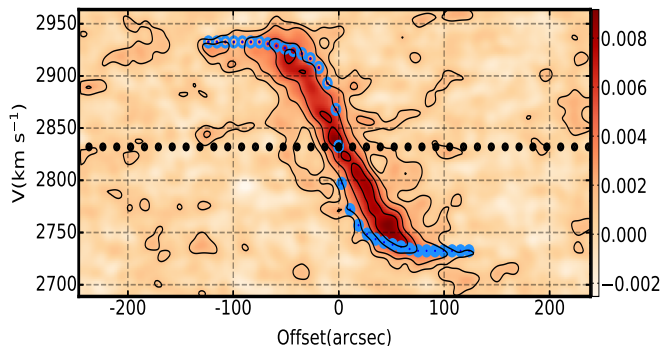


Figure 6. PV diagrams of FGC 2366 derived along the major axis. We have overplotted the rotation curve derived from the 3D tilted ring modelling [blue points]. The contour levels are at $[1.5, 3, 6, 9, 12] \times 0.8 \text{ mJy beam}^{-1}$. The black dotted line indicates the systemic velocity estimated by fitting 3D models to the observed data cube.

5 DYNAMICAL MODELLING

5.1 Mass Modeling

In this section, we determine the contribution of the dark matter halo to the net gravitational potential by decomposing the total rotation curve into baryonic (*stars + gas*) and dark matter components, respectively. The total rotation curve of the galaxy is obtained by adding in quadrature the circular velocity we would have seen if the net gravitational potential was due to each component alone.

$$V_{Total}^2 = (M/L)V_*^2 + V_{Gas}^2 + V_{DM}^2 \quad (1)$$

where M/L is the mass-to-light ratio, V_* , V_{Gas} and V_{DM} are the circular velocity due to the stars, gas, and dark matter

potentials alone, respectively. The observed rotational velocity is determined using tilted ring modelling, as discussed in §3.2. We derive the circular velocity of the gas disc V_{Gas} by modelling the gas disc as thin concentric rings using the GIPSY task ROTMOD (Van der Hulst et al. 1992). We use the average HI surface density of the approaching and the receding side as a function of radius obtained from the tilted ring model (Figure 5, Third Panel) as the input parameter in ROTMOD. The gas surface density is scaled by 1.4 for helium and other metals. Similarly, we derive the circular velocity of the stellar disc using the structural parameters derived from z-band photometry; the structural parameters are given in Table 6. We model the dark matter distribution using the observationally motivated pseudo isothermal (PIS) dark matter halo (Begeman et al. 1991; Fuchs et al. 1998) characterized by a constant density core and, also using the Navarro-Frenk-White (NFW) dark matter halo profile derived from the cold dark matter (CDM) simulations Navarro et al. (1997). The rotation curve of the cored PIS halo is given by

$$V(R) = \sqrt{4\pi G \rho_0 R_c^2 \left(1 - \frac{R_c}{R} \arctan\left(\frac{R}{R_c}\right)\right)} \quad (2)$$

where ρ_0 is the central density of the halo and R_c is the core radius. The rotation curve due to the cuspy NFW density distribution is,

$$V(R) = V_{200} \sqrt{\frac{\ln(1+cx) - cx/(1+cx)}{x[\ln(1+c) - c/(1+c)]}} \quad (3)$$

where $x = R/R_{200}$, R_{200} is the radius at which the mean density of the dark matter halo is 200 times the critical density. V_{200} is the rotation velocity at R_{200} . The concentration pa-

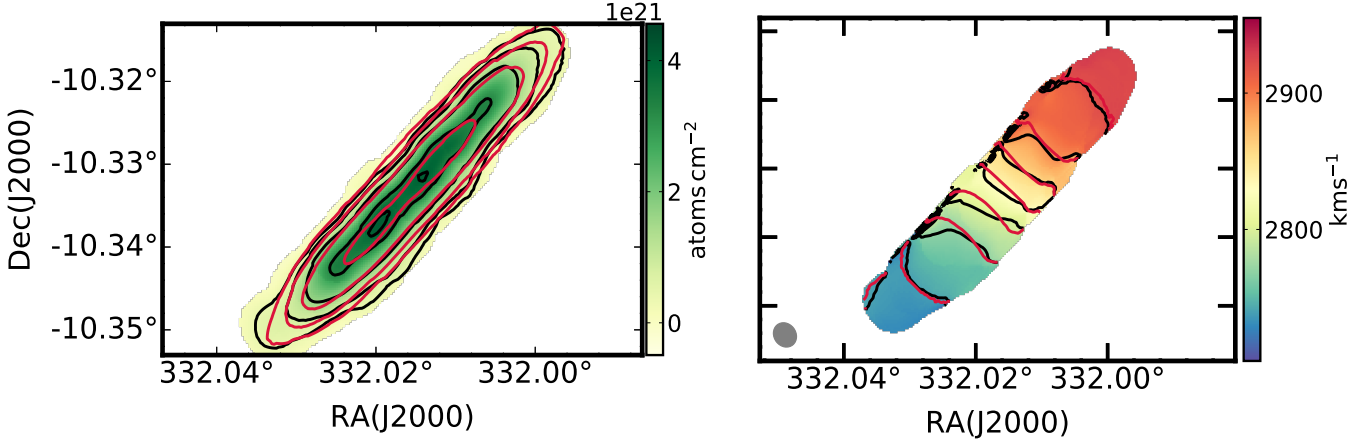


Figure 7. Moment 0 and Moment 1 map derived from the observed and the model HI data cube. The model contours are shown in crimson, and the data contours are shown in black. The contours levels in the moment 0 maps are at $[4, 8, 16, 32, 40] \times 10^{20}$ atoms cm^{-2} and the contour in the Moment 1 map starts at 2951 km s^{-1} and ends at 2710 km s^{-1} , increasing by 26 km s^{-1} .

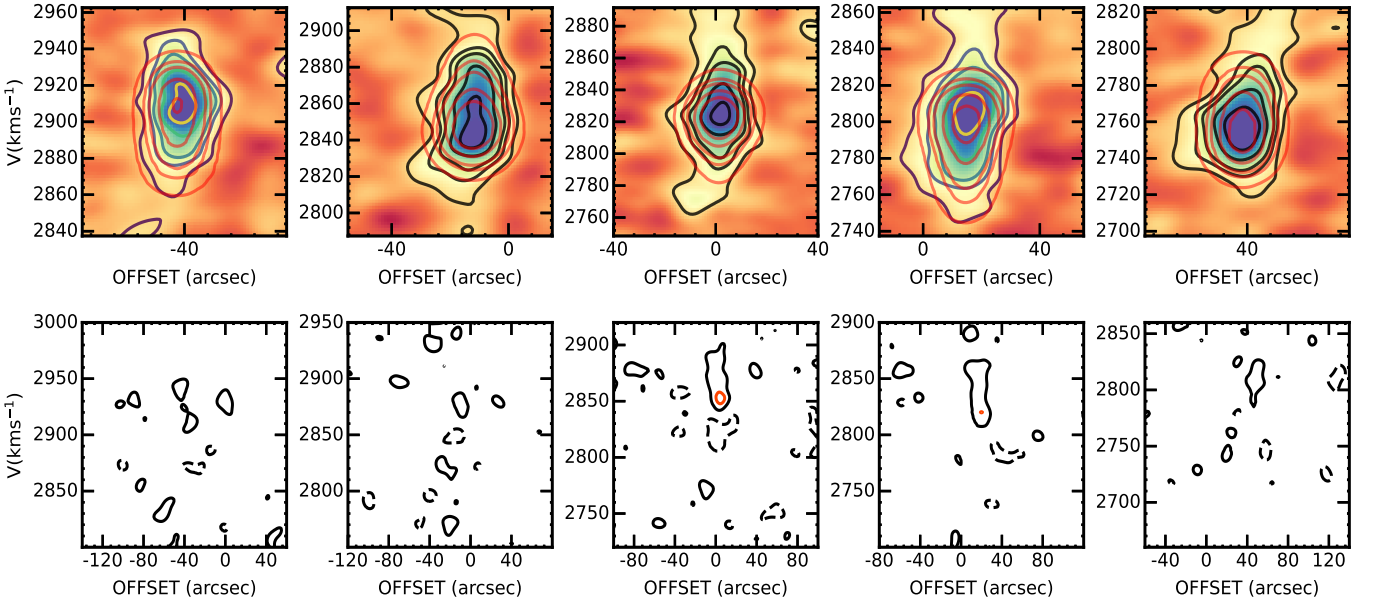


Figure 8. In the top panels, we show the PV diagrams of the observed data cube and the model data cube along the minor axis. The contour levels are at $[1.5, 3, 4, 6, 8] \times 1.0 \text{ mJy beam}^{-1}$. The black contours in the top panel indicate the data, and the red coloured contours correspond to the model. In the bottom panels we plot the residuals corresponding to the minor axis PV diagrams were obtained by subtracting the model from the data.

parameter is defined as $c = R_{200}/R_s$, and R_s is the characteristic scale radius of the NFW density profile.

Finally, the likelihood function is defined as $\exp(-\chi^2/2)$, where χ^2 is given by,

$$\chi^2 = \sum_R \frac{(V_{\text{obs}}(R) - V_{\text{Total}}(R))^2}{V_{\text{err}}^2(R)} \quad (4)$$

where V_{obs} is the observed rotation curve (see left panel Figure 5), V_{Total} is the total rotation curve (see Equation 1), and V_{err} the error bar in V_{obs} . The uncertainty on the observed rotation curve is discussed in §3.2. We use a differential evo-

lution algorithm implemented in the python package Scipy (Virtanen et al. 2020) for finding the maximum likelihood solution. We derive mass models by fixing the value of the stellar mass-to-light ratio derived using the stellar population synthesis models assuming a ‘diet’-Salpeter initial mass function (IMF) (Table 6). The ‘diet’-Salpeter function gives the maximum stellar mass in a photometric band.

Dark Matter Halo:

The results of the mass modelling are presented in Figure 10 and summarized in Table 7. From mass modelling, we find that the cuspy NFW halo ($\chi_{\text{red}}^2 = 0.35$) fits the observed

Table 6. Input parameters for the stellar rotation curve.

| Parameter | Value z-band | Description |
|--|-----------------|---|
| $\mu_o^{face-on(*)}$ | 22.8 | Face-on surface brightness (mag/arcsec ²) |
| Σ_o | 21.5 | Surface density (L_\odot/pc^2) |
| R_d | 2.6 | Disc scalelength (kpc) |
| h_z | 0.29 | Disc scaleheight (kpc) |
| Input parameters for mass-to-light ratio M/L | | |
| $g-z$ | 0.7 | |
| a_λ | -0.17 | Bell et al. (2003a) |
| b_λ | 0.32 | Bell et al. (2003a) |
| M/L | 1.12 | M/L ratio derived using scaled Salpeter IMF |
| M/L | 0.8 | M/L ratio derived using Kroupa IMF |

(*): The edge-on surface brightness has been converted to face-on surface brightness using $\mu^{face-on} = \mu^{edge-on} + 2.5 \log(\frac{R_d}{h_z})$ (Kregel et al. 2005).

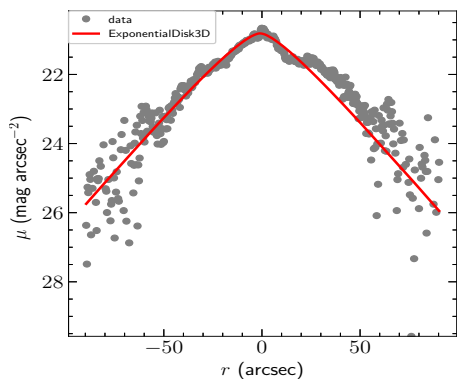


Figure 9. The model and data profiles along the major axis of FGC 2366 for the z-band optical image. The light distribution is modelled using the ExponentialDisk3D function, keeping the surface brightness, scaleheight, scalelength, and inclination as the free parameters.

rotation curve better than the cored PIS halo ($\chi_{red}^2 = 2.4$). Mass models derived using PIS halo are characterized by a small core radius R_c equal to 0.9 kpc, indicating that the baryons in FGC 2366 are embedded in a compact dark matter halo defined as $R_c/R_d < 2$ (Banerjee & Jog 2013a). Mass models employing the NFW halo have a concentration parameter $c \sim 7.9$, higher than the median $c \sim 3.7$ of the ordinary disc galaxies of the THINGS galaxy sample De Blok et al. (2008). In Figure 11, we compare the results obtained from the mass models of FGC 2366 with those of another extremely thin galaxy FGC 1440, and other superthin galaxies for which the mass models were already available in the literature (IC 2233, IC 5249, FGC 1540, UGC 7321). As a function of a/b , we plot (i) the ratio of the core radius of the PIS Dark Matter halo to the stellar disc scalelength R_c/R_d (ii) $V_{rot}/(R_c/R_d)$ where V_{rot} is the asymptotic rotational velocity, and finally (iii) the concentration parameter c from the NFW model with the respective regression lines superposed in each case. We note that, as expected, R_c/R_d decreases with a/b , i.e., a thinner galaxy has a smaller value of R_c/R_d . Banerjee et al. (2010) define a compact halo as one in which $R_c/R_d < 2$. Hence a compact dark matter halo could regulate the galactic disc dynamics from the inner galactocentric radius. Banerjee & Jog (2013a) and Kurapati et al. (2018) argue that a compact dark matter halo is responsi-

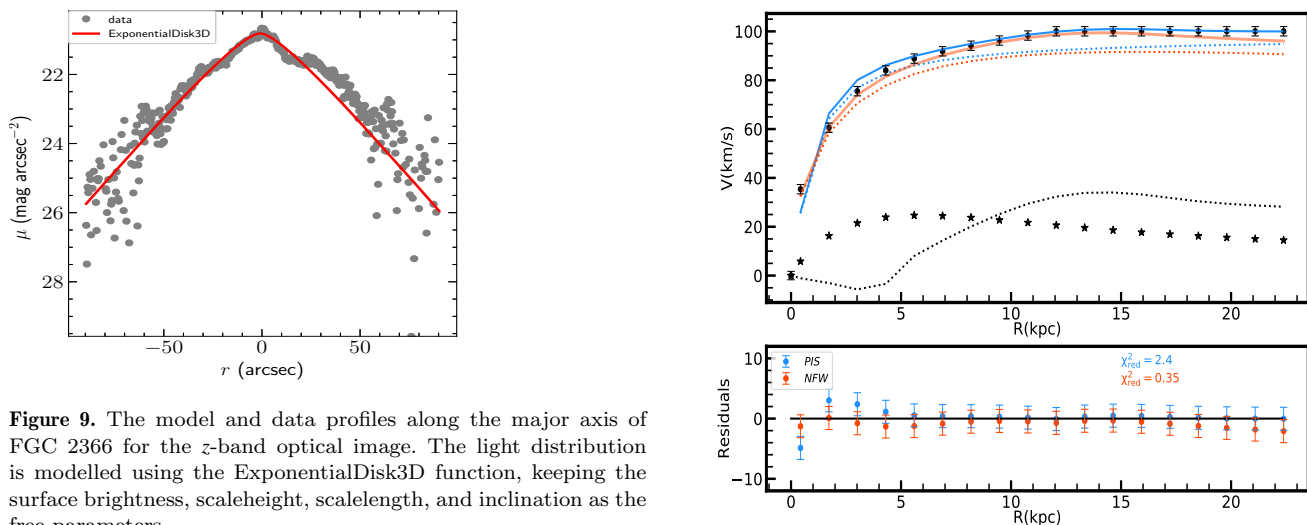


Figure 10. In the top panel, we show the mass-models of the galaxy FGC 2366 derived using SDSS z-band photometry. The mass models are obtained by fixing M/L from population synthesis models using a diet-Salpeter IMF. In the bottom panels, we show the residuals obtained by subtracting the data from the model weighed by the errors on the observed rotation curve. In the top panel, stars and the dashed curve indicate the circular velocities of stars and gas, respectively. The dashed blue and red coloured curves indicate the circular velocity of the dark matter halo using a PIS and NFW models, respectively. Similarly, the solid blue and red lines indicate the total rotation curve assuming a PIS and NFW dark matter model. The black points depict the observed rotation curve.

ble for superthin stellar discs in these galaxies. We further observe that $V_{rot}/(R_c/R_d)$ sharply increases with a/b . V_{rot} is a proxy of the total dynamical mass of the galaxy. In the case of superthin and extremely thin galaxies, the total dynamical mass is dominated by the dark matter halo. Thus $V_{rot}/(R_c/R_d)$ indicates the dark matter dominance in the inner galaxy, i.e., within the stellar disc. Finally, we find that the galaxies with a larger a/b have larger values of c , indicating that thinner galaxies have higher concentration parameters in line with the findings of Banerjee et al. (2010).

With the total mass inventory in place, we proceed to derive the dynamical models of FGC 2366 by using first the

Table 7. Dark matter density profiles derived from mass-models

| Model | $c^{(a)}$ | $R_{200}^{(b)}$ (kpc) | $M/L^{(c)}$ | $\chi_{red}^{2(d)}$ | $\rho_0^{(e)} \times 10^{-3}$ M_\odot/pc^3 | $R_c^{(f)}$ (kpc) | $M/L^{(g)}$ | $\chi_{red}^{2(h)}$ |
|-----------------|---------------|--------------------------|-------------|---------------------|---|----------------------|-------------|---------------------|
| z-band | NFW profile | | | | PIS profile | | | |
| 'diet' Salpeter | 7.9 ± 0.2 | 58.3 ± 0.4 | 1.1 | 0.35 | 217.8 ± 40.2 | 0.9 ± 0.09 | 1.1 | 2.4 |

(a): Concentration parameter of the NFW profile

(b): Radius at which the mean density equals 200 times the critical density.

(c): Mass to light ratio derived using population synthesis models or estimated as a free parameter.

(d): Reduced chi-square value corresponding to the fit.

(e): The central dark matter density of the PIS dark matter halo model

(f): The core radius of the PIS dark matter halo model

(g): Mass to light ratio derived using population synthesis models or estimated as a free parameter.

(h): Reduced chi-square value corresponding to the fit.

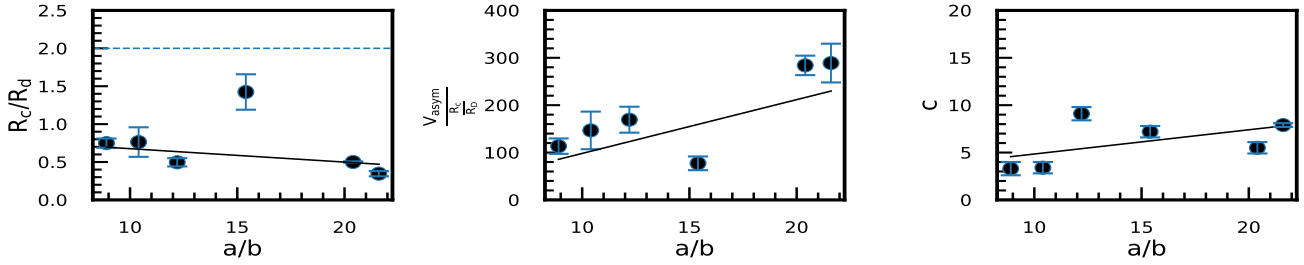


Figure 11. For a sample of superthin and extremely thin galaxies including FGC 2366, we plot the ratio of the dark matter core radius to the disc scale length R_c/R_d indicating its compactness in the left panel, the ratio of asymptotic rotation velocity (V_{asym}) to the compactness parameter (R_c/R_d) indicating the compactness of the mass distribution versus a/b in the middle panel, and the dark matter concentration c , versus a/b in third panel. In left panel, the horizontal the line indicates the limiting value of R_c/R_d for a compact halo. Superimposed on the data points in each panel is the best-fitting regression line. The last two points in each panel represent the extremely thin galaxies FGC 1440 and FGC 2366, respectively.

2-component model of gravitationally-coupled stars + gas in the force field of the dark matter halo (See [Aditya & Banerjee \(2021\)](#), for details). In the case of the 2-component model, we can not derive the radial velocity dispersion as the thin disc approximation, and several other simplifying assumptions decouple the vertical and radial motions. However, it can be used to derive the stellar vertical velocity dispersion using the stellar vertical scale height as a constraint. Next, we use this stellar vertical velocity dispersion as an initial input. We set up the distribution function-based equilibrium models using AGAMA ([Vasiliev 2019](#)) to derive the radial velocity dispersion and the stellar vertical scale height. If the latter matches the observed scaleheight, we conclude that the 2-component model and the Self-consistent model (SCM) are consistent.

5.2 Self-consistent model of the stellar disc using AGAMA:

We model the dynamics of FGC 2366 in dynamical equilibrium using the multi-component, self-consistent, iterative modelling method ([Binney 2014](#); [Piffl et al. 2015](#)) implemented in AGAMA ([Vasiliev 2018](#)) in order to derive the vertical and the radial velocity dispersion of the stars. We model FGC 2366 as a 2-component system of the stars and the dark matter halo in the force field of the HI gas. The stellar and the dark matter halo are defined by their distribution functions conforming to their corresponding density profiles; HI is included as a static density component using

the parameters from the tilted-ring models (§3.2). The details of the model profile are discussed below. We model the stellar disc with an exponential surface density consistent with the parameters obtained from the optical photometry. We model the stellar distribution function using the quasi-isothermal distribution function.

The stellar density profile is given by

$$\Sigma_s(R) = \Sigma_{0,s} e^{-\frac{R}{R_{d,s}}} e^{-\frac{z}{h_{z,s}}} \quad (5)$$

where, $\Sigma_{0,s}$ is the central stellar density, $R_{d,s}$ is the disc scale-length and $h_{z,s}$ is the exponential scaleheight. The quasi-isothermal distribution function for the stellar disc is given as follows:

$$f(J) = f_0(J_\phi) \frac{\kappa}{\sigma_R^2} e^{-\frac{\kappa J_R}{\sigma_R^2}} \frac{\nu}{\sigma_z^2} e^{-\frac{\nu J_z}{\sigma_z^2}} \quad (6)$$

where κ and ν are the radial and vertical epicyclic frequencies, respectively. σ_R and σ_z are the stellar velocity dispersion in the respective directions. J_R , J_z , and J_ϕ are the actions of the stellar discs in the corresponding directions. Here, $J_\phi^2 = R^3 \frac{\partial \Phi}{\partial R}$, $J^2 = J_R^2 + J_\phi^2 + J_z^2$ and $f_0(J_\phi) = \frac{\Sigma(R)\Omega(R)}{2\pi^2 \kappa^2(R)}$, where Φ and Ω are the total gravitational potential and angular velocity respectively. The radial dependence of the velocity dispersion in the radial and vertical directions is modelled as

$$\begin{aligned}\sigma_R(R) &= \sigma_{R,0} e^{\frac{-R}{R_{\sigma_R}}} \\ \sigma_z(R) &= \sigma_{z,0} e^{\frac{-R}{R_{\sigma_z}}}\end{aligned}\quad (7)$$

where R_{σ_R} and R_{σ_z} are the scale lengths in the radial and the vertical directions, respectively.

The HI density is modelled as a static potential as follows:

$$\Sigma_g(R) = \Sigma_{0,g} e^{-\left(\frac{R}{a_g}\right)^2} \quad (8)$$

where the values of $\Sigma_{0,g}$ and a_g are obtained by fitting the HI surface density derived from our HI observations using the tilted ring modelling (see Figure 5).

The dark matter, modelled as a 3-parameter spherically-symmetric function, is given by:

$$\rho_r = \rho_0 (r/a)^{-\gamma} \left(1 + \left(\frac{r}{a}\right)^\alpha\right)^{\left(\frac{\gamma-\beta}{\alpha}\right)} \quad (9)$$

We use $\alpha = 1$, $\beta = 3$, $\gamma = 1$, in the above to mimic the cuspy NFW profile, where ρ_0 is the central density and a is the characteristic scale of the NFW halo given by $a = R_{200}/c$. Similarly, if we set $\alpha = 2$, $\beta = 2$, $\gamma = 0$, for the cored PIS halo, a mimics the core radius of the density profile and ρ_0 the value central density. We derive the distribution function for the dark matter halo corresponding to the input density profile by the *Quasi-Spherical* distribution instance implemented in AGAMA. It constructs the distribution function using the input density profile using the generalized Eddington inversion formula. It then uses a spherical action finder to convert the distribution function into an action-based form. The values for the dark matter density for the PIS and NFW halo are taken from the mass model derived in §5 (Table 7). We use the value of the stellar vertical velocity dispersion obtained from the 2-component method (See Aditya & Banerjee (2021)) as input for constructing the self-consistent models using AGAMA. We start by creating an initial guess for the total potential of FGC 2366 using the results obtained from tilted ring modeling, optical photometry, and mass models. We then construct actions corresponding to this potential using the "action-finder" implemented in AGAMA and compute the distribution function and the density from the distribution function. We again calculate the updated potential by solving Poisson's equation for the combined density of all the terms. We then repeat the above procedure of calculating the actions from the updated potential and evaluate the distribution function at every step. We compute the density from the distribution function and calculate the potential until the potential converges.

Stellar velocity dispersions

In Figure 12, we present the best-fitting SCM for FGC 2366 obtained using the NFW dark matter profile, which has a smaller value of the reduced χ^2 than the PIS model. We note that the central vertical stellar velocity dispersion $\sigma_{z,0} = 23 \text{ km s}^{-1}$ is comparable to that of the Milky Way thin disc ($\sigma_{z,0} = 25 \text{ km s}^{-1}$) (Sharma et al. 2014).

Interestingly, the value of $\sigma_{R,0} = 61 \text{ km s}^{-1}$ for FGC 2366 is higher than the value of $\sigma_{R,0} = 40 \text{ km s}^{-1}$ obtained for

Milky Way. (Sharma et al. 2014; Bovy et al. 2012). In Figure 13, we present $\text{Min}(\sigma_z/\sigma_R)$ as a function of a/b for our galaxy sample, overlaying the corresponding regression line. A small value of σ_z/σ_R indicates that the excursion of the stars from their mean vertical position in the galactic mid-plane is smaller than their dispersion about a mean radius in the plane. For field galaxies like the superthin, an increase in σ_z is a reflection of disc thickening due to vertical bending instabilities and counter-rotating bars among others (Khoperskov et al. 2003; Khoperskov & Bertin 2017); a large value of σ_R , on the other hand, is attributed to disc heating by bars and spiral arms, and also to radial migration of stars (Roškar et al. 2013). Jenkins & Binney (1990) shows that the relatively higher rate of dynamical heating in the plane renders the value of σ_z/σ_R smaller. Due to the edge-on orientation of these galaxies, it is not possible to ascertain the presence of the spiral structure in their plane. Thus it leaves the question regarding the dynamical origin of the high anisotropy of the stellar velocity ellipsoid in these galaxies.

Disc dynamical stability of FGC 2366

Since a hotter disc is dynamically stabler, the σ_R value obtained above partially regulates the dynamical stability of the galactic discs, and therefore possibly their razor-thin morphology. We use the multi-component stability parameter proposed by Romeo & Wiegert (2011):

$$\frac{1}{Q_{RW}} = \begin{cases} \frac{W_\sigma}{T_s Q_s} + \frac{1}{T_g Q_g} & \text{if } T_s Q_s > T_g Q_g \\ \frac{1}{T_s Q_s} + \frac{W_\sigma}{T_g Q_g} & \text{if } T_s Q_s < T_g Q_g \end{cases} \quad (10)$$

where the weight function W_σ is given by

$$W_\sigma = \frac{2\sigma_s \sigma_g}{\sigma_s^2 + \sigma_g^2} \quad (11)$$

,the thickness correction defined as

$$T \approx 0.8 + 0.7 \frac{\sigma_z}{\sigma_R} \quad (12)$$

and the Toomre Q parameters of the stellar and the gaseous discs are given by $Q = \frac{\kappa \sigma}{\pi G \Sigma}$, where κ is the epicyclic frequency, and Σ the surface density. The σ_R , σ_z and hence σ_s values were estimated from self-consistent iterative modelling in section 5.2, and σ_g from the tilted ring modelling from section 3.2. A value of $Q_{RW} > 1$ should indicate that the disc is stable against the growth of local axisymmetric perturbations. However, numerical studies have shown that in non-axisymmetric perturbations, a $Q_{RW} \sim 2-3$ indicates a stable disc. We have presented the Q_{RW} as a function of R for FGC 2366 in Figure 14. The minimum value of $Q_{RW} = 3.1$ indicates that the disc is very stable against the growth of axisymmetric instabilities. In Figure 15, we compare the Q_{RW} values at $1.5R_d$ of the extremely thin galaxy FGC 2366 with a previously studied sample of superthin galaxies and with another extremely thin galaxy FGC 1440. The corresponding regression line in Figure 16 indicates that the values of Q_{RW} at $1.5R_d$ increase with a/b , indicating that the galaxies with the thinnest discs have the highest disc dynamical stability values; see also, Garg & Banerjee (2017).

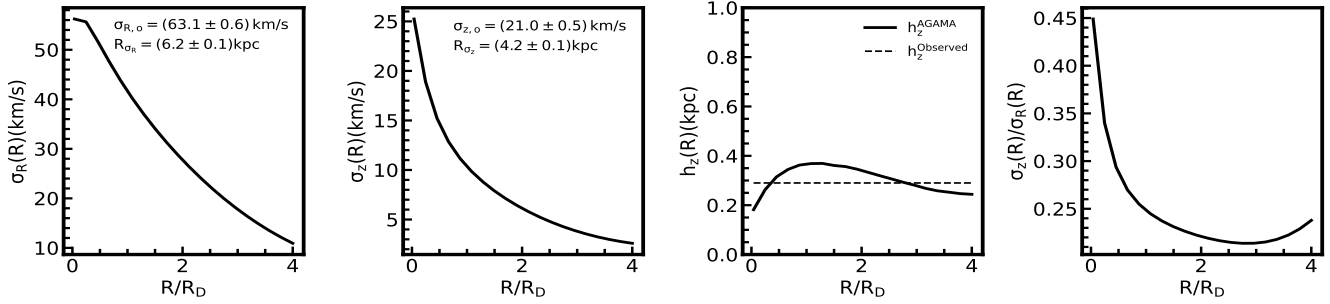


Figure 12. In first panel, we show the stellar radial velocity dispersion, in panel 2, we plot the stellar vertical velocity dispersion, in the third panel, we show the stellar scaleheight, and in the fourth panel we show the ratio of vertical-to-radial stellar velocity dispersion, as a function of galactocentric radius normalized by disc scale length, as determined by dynamical modelling with an NFW dark matter halo using AGAMA for FGC 2366. The dotted line in third panel shows the observed scale height.

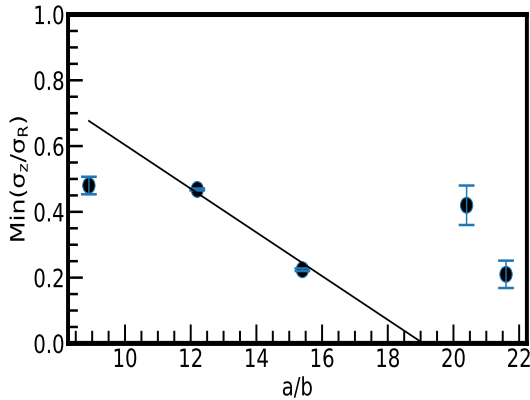


Figure 13. Ratio of the vertical-to-radial stellar velocity dispersion as a function of the major-to-minor axes ratio derived from dynamical models for a sample of superthin and extremely thin galaxies, including FGC 2366. The regression line is superposed. The last two points in the plot represent the extremely thin galaxies FGC 1440 and FGC 2366, respectively.

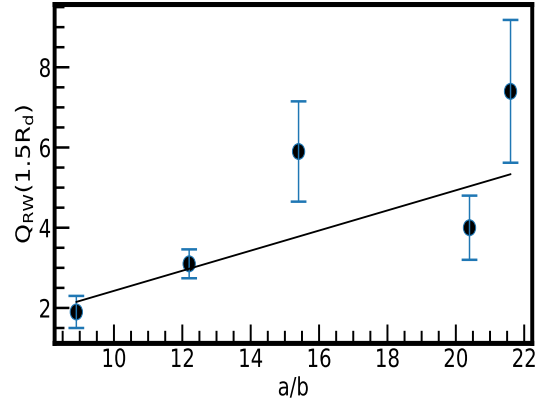


Figure 15. 2-component disc dynamical stability parameter Q_{RW} at $R = 1.5R_d$ as a function of the major-to-minor axes ratio a/b for a sample of superthin and extremely thin galaxies including FGC 2366. The last two points represent the extremely thin galaxies FGC 1440 and FGC 2366, respectively.

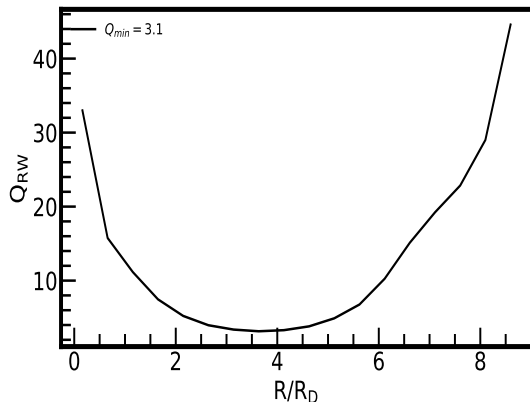


Figure 14. 2-component disc dynamical stability parameter Q_{RW} as a function of R/R_D for FGC 2366 as obtained from AGAMA.

Specific angular momentum

The specific angular momentum j_i of the i^{th} component of the disc may be given by

$$j_i(R) = \frac{2\pi \int_0^R R'^2 \Sigma_i(R') V(R') dR'}{2\pi \int_0^R R' \Sigma_i(R') dR'} \quad (13)$$

where $\Sigma_i(R')$ corresponds to the surface density of the i^{th} component, and V the asymptotic rotational velocity. In Figure 16, we present the $j^* - M$ relation for ordinary bulgeless disc galaxies as derived by [Jadhav Y & Banerjee \(2019\)](#), and also that of a sample of disc galaxies spanning a large mass range $7 \leq \log(M_*/M_\odot) \leq 11.5$ and $6 \leq \log(M_{\text{gas}}/M_\odot) \leq 11$ as obtained by [Mancera Piña et al. \(2021\)](#). We superpose on them the data points for FGC 2366 along with another extremely thin galaxy, FGC 1440 studied earlier, and also those of the sample of superthins from [Jadhav Y & Banerjee \(2019\)](#). Unlike FGC 1440, we note that FGC 2366 lies above the 95.4% confidence intervals of both the $j^* - M_*$ relations, similar to the trend in other superthin galaxies. Figure 17, we plot j_* as a

Table 8. Dynamical parameters of FGC 2366 as obtained using AGAMA

| Parameter | Value |
|---------------------------------------|-----------------|
| R_c/R_d | 0.35 ± 0.03 |
| $V_{\text{rot}}/(R_c/R_d)$ | 288 ± 40 |
| σ_z/σ_R | 0.2 ± 0.04 |
| $Q_{RW}(1.5R_d)$ | 7.0 ± 1.8 |
| $\log_{10}(j_*/\text{kpc km s}^{-1})$ | 2.67 ± 0.02 |

function of a/b for the sample of superthins studied earlier along with FGC 1440 and FGC 2366. The regression line fit indicates that j_* increases with a/b , meaning thinner discs may have higher specific angular momentum.

Principal Component Analysis

Finally, we attempt to understand the physical factor primarily driving the vertical structure of the stellar discs in superthin galaxies, the possible parameters being j_* , $Q_{RW}(1.5R_d)$, $\text{Min}(\sigma_z/\sigma_R)$, for the stars $V_{\text{rot}}/(R_c/R_d)$ along with a/b . In Table 8, we present the same for FGC 2366 as calculated from the dynamical models obtained in this paper. The same can be obtained for all the superthins studied earlier and the extremely thin galaxy FGC 1440. Since we have less than ten galaxies in our sample (IC 2233, FGC 1540, UGC 7321, FGC 1440, & FGC 2366), we create ~ 1000 mock galaxies from each galaxy of our sample as follows. For each galaxy, we construct a 5-D Gaussian distribution of the parameters using the best-fitting value of each parameter as the mean and the error as the standard deviation for the corresponding distribution. We then randomly sample 1000 points from this 5-D parameter space which serve as the mock galaxies. We repeat this process for each galaxy in our sample. We next carry out a Principal Component Analysis (PCA) of the parameters: j_* , $Q_{RW}(1.5R_d)$, $\text{Min}(\sigma_z/\sigma_R)$, $V_{\text{rot}}/(R_c/R_d)$ along with a/b . The principal components (PCs) are presented in Figure 18. In Figure 19, we present the decomposition of the PCs in terms of the different parameters. We note that the contributions from a/b , $V_{\text{rot}}/R_c/RD$ and Q_{RW} is the maximum for PC1 and PC2 taken together and explains 88% of the variation in data. This possibly indicates that the major driving factor for the superthin vertical structure is the dark matter dominance at inner galactocentric radii as indicated by $V_{\text{rot}}/(R_c/R_d)$.

6 CONCLUSIONS

In this paper, we present GMRT HI 21cm radio-synthesis observations of an edge-on low surface brightness galaxy FGC 2366 with the largest axial ratio $a/b = 21.6$ and hence the thinnest stellar disc. We carry out the data reduction using CASA and employ the 3-D tilted ring modelling to derive the kinematics and structural properties of neutral HI distribution. *We note that HI distribution is uniform and unperturbed and does not show a signature of warping or flaring in FGC 2366.*

We also present the optical photometry in the g , r and z bands. Using the total HI rotation curve along with the z -band optical photometry, we next derive its mass

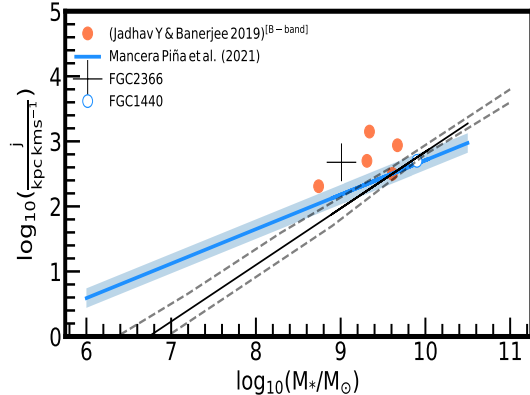


Figure 16. Comparison of the specific angular momentum of stars in FGC 2366 with a sample of previously studied superthin galaxies and the extremely thin galaxy FGC 1440. The ‘blue’ regression line is for a sample of disc galaxies studied by Mancera Piña et al. (2021). The solid black line shows the regression line obtained by Jadhav Y & Banerjee (2019) for a sample of six ordinary bulgeless disc galaxies with bulge fraction less than 0.05 from a larger sample of disc galaxies studied by Obreschkow & Glazebrook (2014). The dashed line shows the 95.4 % confidence interval on the regression line obtained by Jadhav Y & Banerjee (2019).

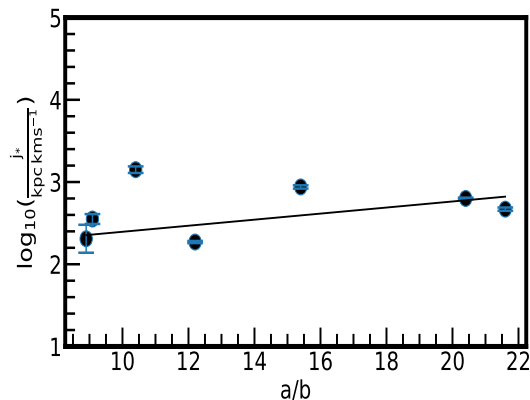


Figure 17. Stellar specific angular momenta j_* as a function of the major-to-minor axes ratio a/b with a sample of previously studied superthin galaxies and the extremely thin galaxy FGC 1440. The last two points represent the extremely thin galaxies FGC 1440 and FGC 2366, respectively.

model, and, after that, we construct the dynamical model of the stellar disc and the dark matter halo using the distribution-function-based stellar dynamical code AGAMA using a quasi-isothermal distribution function to represent the stars and a quasi-Spherical one for dark matter halo. *We find that the NFW dark matter halo gives a better fit to the steeply rising rotation curve of FGC 2366.*

Finally, we consider a set of parameters obtained from the dynamical model constructed that may be responsible for the superthin vertical structure of the stellar discs: the specific angular momentum of the stellar disc j_* , the 2-

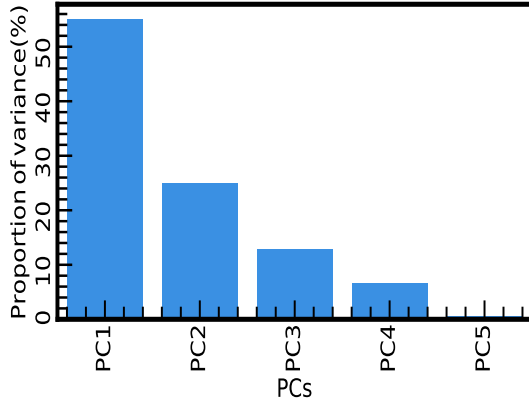


Figure 18. Scree plot from the principal component analysis of the dynamical parameters plausibly responsible for driving the superthin stellar discs.

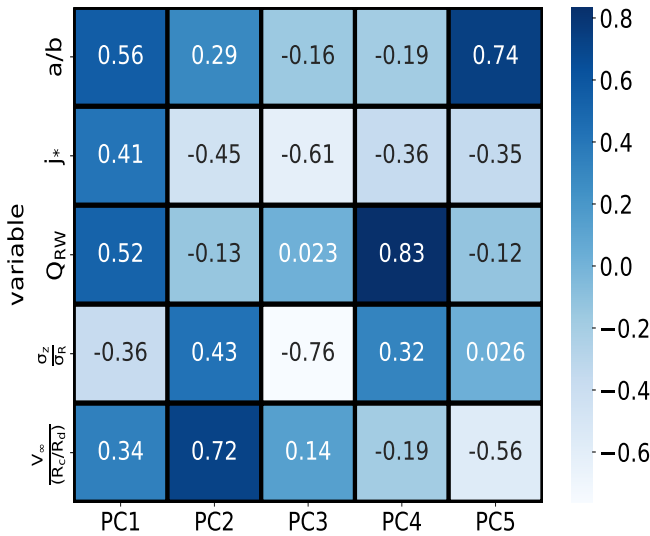


Figure 19. Loadings of the Principal Component Analysis of the dynamical parameters plausibly responsible for driving the superthin stellar discs.

component disc stability parameter at $R = 1.5R_d$ $Q_{RW}(1.5R_d)$, the ratio of the central values of the stellar vertical velocity dispersion -to-the-radial velocity dispersion $\text{Min}(\sigma_z/\sigma_R)$, and the compactness of the mass distribution $V_{rot}/(R_c/R_d)$. In order to identify the dynamical parameter/s crucial for the existence of the superthin vertical structure, we carry out a Principal Component Analysis (PCA) of the above parameters corresponding to a sample of superthin galaxies and the extremely thin galaxy FGC 1440 studied in the past along with those of FGC 2366. We found that the variance in the values of the above parameters was mostly explained by $V_{rot}/(R_c/R_d)$. *We, therefore, conclude that the compactness of the mass distribution is fundamentally responsible for a superthin stellar vertical structure.*

7 DATA AVAILABILITY

The data from this study are available upon request.

8 ACKNOWLEDGEMENT

We thank the staff of the GMRT that made these observations possible. GMRT is run by the National Centre for Radio Astrophysics of the Tata Institute of Fundamental Research. Aditya would like to thank Dr. Eugene Vasiliev for help with AGAMA. PK is partially supported by the BMBF project 05A20PC4 for D-MeerKAT. SB and DM acknowledge the support by the Russian Science Foundation, grant 19-12-00145. We acknowledge the usage of the HyperLeda database. (<http://leda.univ-lyon1.fr>). We also thank Dr. K. Saikranthi for the helpful discussion.

REFERENCES

- Aditya K., Banerjee A., 2021, *Monthly Notices of the Royal Astronomical Society*
- Banerjee A., Bapat D., 2017, *Monthly Notices of the Royal Astronomical Society*, 466, 3753
- Banerjee A., Jog C. J., 2013a, *Monthly Notices of the Royal Astronomical Society*, 431, 582
- Banerjee A., Jog C. J., 2013b, *Monthly Notices of the Royal Astronomical Society*, 431, 582
- Banerjee A., Matthews L. D., Jog C. J., 2010, *New Astronomy*, 15, 89
- Begman K., Broeils A., Sanders R., 1991, *Monthly Notices of the Royal Astronomical Society*, 249, 523
- Bell E. F., McIntosh D. H., Katz N., Weinberg M. D., 2003a, *The Astrophysical Journal Supplement Series*, 149, 289
- Bell E. F., McIntosh D. H., Katz N., Weinberg M. D., 2003b, *The Astrophysical Journal Supplement Series*, 149, 289
- Binney J., 2014, *Monthly Notices of the Royal Astronomical Society*, 440, 787
- Bizyaev D., Kautsch S., Sotnikova N. Y., Reshetnikov V. P., Mosenkov A. V., 2017, *Monthly Notices of the Royal Astronomical Society*, 465, 3784
- Bizyaev D., Makarov D. I., Reshetnikov V. P., Mosenkov A. V., Kautsch S. J., Antipova A. V., 2021, *The Astrophysical Journal*, 914, 104
- Bothun G., Impey C., McGaugh S., 1997, *Publications of the Astronomical Society of the Pacific*, 109, 745
- Bottrell C., Torrey P., Simard L., Ellison S. L., 2017, *Monthly Notices of the Royal Astronomical Society*, 467, 2879
- Bovy J., et al., 2012, *The Astrophysical Journal*, 759, 131
- De Blok W., Walter F., Brinks E., Trachternach C., Oh S., Kennicutt Jr R., 2008, *The Astronomical Journal*, 136, 2648
- Dey A., et al., 2019, *The Astronomical Journal*, 157, 168
- Erwin P., 2015, *The Astrophysical Journal*, 799, 226
- Fuchs B., Möllenhoff C., Heidt H., 1998, *Astronomy and Astrophysics*, 336, 878
- Garg P., Banerjee A., 2017, *Monthly Notices of the Royal Astronomical Society*, 472, 166
- Gentile G., et al., 2015, *Astronomy & Astrophysics*, 576, A57
- Ghosh S., Jog C. J., 2014, *Monthly Notices of the Royal Astronomical Society*, 439, 929
- Goad J., Roberts M., 1981, *The Astrophysical Journal*, 250, 79
- Grand R. J., Springel V., Gómez F. A., Marinacci F., Pakmor R., Campbell D. J., Jenkins A., 2016, *Monthly Notices of the Royal Astronomical Society*, 459, 199
- Haslbauer M., Banik I., Kroupa P., Wittenburg N., Javanmardi B., 2022, *The Astrophysical Journal*, 925, 183

- Jadhav Y V., Banerjee A., 2019, *Monthly Notices of the Royal Astronomical Society*, 488, 547
- Jenkins A., Binney J., 1990, *Monthly Notices of the Royal Astronomical Society*, 245, 305
- Józsa G. I. G., Kenn F., Klein U., Oosterloo T. A., 2007, *Astronomy & Astrophysics*, 468, 731
- Kamphuis P., Józsa G., Oh S.-H., Spekkens K., Urbancic N., Serra P., Koribalski B., Dettmar R.-J., 2015, *Monthly Notices of the Royal Astronomical Society*, 452, 3139
- Karachentsev I. D., Karachentseva V. E., Kudrya Y. N., Sharina M. E., Parnovskij S. L., 1999, *Bulletin of the Special Astrophysics Observatory*, 47, 5
- Karachentseva V., Kudrya Y. N., Karachentsev I., Makarov D., Melnyk O., 2016, *Astrophysical Bulletin*, 71, 1
- Kautsch S. J., 2009, *Publications of the Astronomical Society of the Pacific*, 121, 1297
- Kautsch S., Grebel E., Barazza F., Gallagher J., 2006, *Astronomy & Astrophysics*, 445, 765
- Khoperskov S., Bertin G., 2017, *Astronomy & Astrophysics*, 597, A103
- Khoperskov A., Zasov A., Tyurina N., 2003, *Astronomy Reports*, 47, 357
- Kourkchi E., Courtois H. M., Graziani R., Hoffman Y., Pomarède D., Shaya E. J., Tully R. B., 2020, *The Astronomical Journal*, 159, 67
- Kregel M., Van Der Kruit P., Freeman K., 2005, *Monthly Notices of the Royal Astronomical Society*, 358, 503
- Kurapati S., Banerjee A., Chengalur J. N., Makarov D., Borisov S., Afanasiev A., Antipova A., 2018, *Monthly Notices of the Royal Astronomical Society*, 479, 5686
- Makarov D., Prugniel P., Terekhova N., Courtois H., Vauglin I., 2014, *Astronomy & Astrophysics*, 570, A13
- Mancera Piña P. E., Posti L., Fraternali F., Adams E. A. K., Oosterloo T., 2021, *Astronomy & Astrophysics*, 647, A76
- Matthew L. D., van Driel W., Gallagher J. S., 2000, in Hammer F., Thuan T. X., Cayatte V., Guiderdoni B., Thanh Van J. T., eds, *Building Galaxies; from the Primordial Universe to the Present*. p. 107
- Matthews L., Uson J. M., 2008, *The Astrophysical Journal*, 688, 237
- Matthews L., van Driel W., 2000, *Astronomy and Astrophysics Supplement Series*, 143, 421
- Matthews L., Gallagher III J., Van Driel W., 1999, *The Astronomical Journal*, 118, 2751
- McGaugh S. S., 1996, *Monthly Notices of the Royal Astronomical Society*, 280, 337
- McGaugh S. S., Schombert J. M., 2014, *The Astronomical Journal*, 148, 77
- McMullin J. P., Waters B., Schiebel D., Young W., Golap K., 2007, in *Astronomical data analysis software and systems XVI*. p. 127
- Narayan C. A., Jog C. J., 2002, *Astronomy & Astrophysics*, 390, L35
- Navarro J. F., Frenk C. S., White S. D., 1997, *The Astrophysical Journal*, 490, 493
- O'Brien J. C., Freeman K., van der Kruit P., 2010, *Astronomy & Astrophysics*, 515, A62
- Obreschkow D., Glazebrook K., 2014, *The Astrophysical Journal*, 784, 26
- Olling R. P., 1995, *The Astronomical Journal*, 110, 591
- Palunas P., Williams T., 2000, *The Astronomical Journal*, 120, 2884
- Piffi T., Penoyre Z., Binney J., 2015, *Monthly Notices of the Royal Astronomical Society*, 451, 639
- Pillepich A., et al., 2018, *Monthly Notices of the Royal Astronomical Society*, 473, 4077
- Purcell C. W., Bullock J. S., Kazantzidis S., 2010, *Monthly Notices of the Royal Astronomical Society*, 404, 1711
- Quinn P., Hernquist L., Fullagar D., 1993, *The Astrophysical Journal*, 403, 74
- Romanowsky A. J., Fall S. M., 2012, *The Astrophysical Journal Supplement Series*, 203, 17
- Romeo A. B., Wiegert J., 2011, *Monthly Notices of the Royal Astronomical Society*, 416, 1191
- Roškar R., Debattista V. P., Loebman S. R., 2013, *Monthly Notices of the Royal Astronomical Society*, 433, 976
- Schaye J., et al., 2015, *Monthly Notices of the Royal Astronomical Society*, 446, 521
- Schlaflly E. F., Finkbeiner D. P., 2011, *The Astrophysical Journal*, 737, 103
- Serra P., et al., 2015, *Monthly Notices of the Royal Astronomical Society*, 448, 1922
- Sharma S., et al., 2014, *The Astrophysical Journal*, 793, 51
- Swaters R., Sancisi R., Van Albada T., Van Der Hulst J., 2009, *Astronomy & Astrophysics*, 493, 871
- Van der Hulst J., Terlouw J., Begeman K., Zwitter W., Roelofsema P., 1992, in *Astronomical Data Analysis Software and Systems I*. p. 131
- Vasiliev E., 2018, *Monthly Notices of the Royal Astronomical Society*, 482, 1525
- Vasiliev E., 2019, *Monthly Notices of the Royal Astronomical Society*, 482, 1525
- Virtanen P., et al., 2020, *Nature methods*, 17, 261
- Vogelsberger M., et al., 2014, *Monthly Notices of the Royal Astronomical Society*, 444, 1518
- Westmeier T., Jurek R., Obreschkow D., Koribalski B. S., Staveley-Smith L., 2014, *Monthly Notices of the Royal Astronomical Society*, 438, 1176
- Zasov A., Makarov D., Mikhailova E., 1991, *Soviet Astronomy Letters*, 17, 374
- van der Kruit P., Jiménez-Vicente J., Kregel M., Freeman K., 2001, *Astronomy & Astrophysics*, 379, 374

9 APPENDIX - A

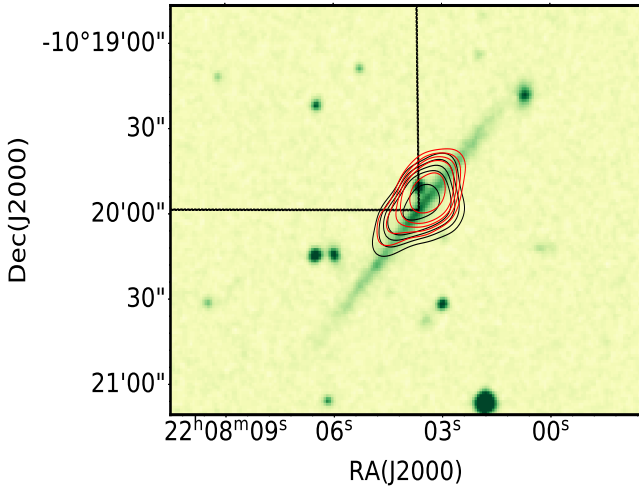


Figure 20. Channel maps showing HI emission from FGC 2366. The black contours show the emissions observed at 2832.5 km s^{-1} , which is systemic velocity obtained by fitting the 3D model to the observed data cube. The red contours, on the other hand, represent the emissions at 2844 km s^{-1} which is obtained by fitting the busy function to the 1D spectrum derived from the data cube. The emissions at 2832.5 km s^{-1} coincide with the centre of the optical image than the emissions at 2844 km s^{-1} . The contour levels are at $[3, 4, 5, 6, 9] \times 0.8 \text{ mJy beam}^{-1}$